optica

High-power picosecond deep-UV source via group velocity matched frequency conversion

Benjamin Willenberg,*,† Fabian Brunner,† [ID] Christopher R. Phillips, [ID] and Ursula Keller [ID]

Department of Physics, ETH Zurich, 8093 Zurich, Switzerland
Corresponding author: bwillenb@phys.ethz.ch

Powerful ultrashort pulses in the deep-ultraviolet (deep-UV) are beneficial for diverse applications from fundamental science to industrial materials processing. However, reaching high powers via conventional approaches is challenging due to three central issues: dispersion, multiphoton absorption, and optical damage. Here, we simultaneously overcome these issues with a novel fifth-harmonic generation architecture optimized for group velocity matching. We use tilted pulse fronts, including a noncollinear geometry in the final sum-frequency generation stage. This enables lower intensities and longer crystals, thereby favoring the birefringently phase matched $\chi^{(2)}$ process over higher-order multiphoton absorption processes. Moreover, we demonstrate low-loss cascaded $\chi^{(2)}$-based spatiotemporal flattening of the input pulses, which enhances the uniformity of the conversion efficiency throughout the beam profile. Through these techniques, we realize a picosecond deep-UV generation source at 206 nm with record-high 2.5 W average output power and a repetition rate of 100 kHz. This result paves the way for a new era of high-power ultrafast deep-UV lasers. © 2020

https://doi.org/10.1364/OPTICA.386257

1. INTRODUCTION

The development of high-repetition-rate deep-ultraviolet (deep-UV) laser sources providing short and powerful light pulses in the picosecond regime is of great interest for applications in materials processing and in scientific studies. The short wavelength enables high spatial resolution and rapid absorption even in wide bandgap materials. When combined with ultrashort pulses for cold ablation, very precise material processing with a minimal heat affected zone can be achieved [1,2]. The energy of a single deep-UV photon can directly break chemical bonds. This process is known as photochemical interaction and enables another type of material processing [3]. Likewise, the energy of a single photon can initiate dissociation of gas phase molecules [4]. Moreover, since the photon energy is higher than the work function of any metal, deep-UV radiation can be used to seed free electron lasers with short bursts of electrons at high repetition rate [5].

Our current motivation is light–matter interaction studies on hydrogen atoms, including the attoclock technique [6,7], which require a high flux of sub-210-nm photons to obtain a cold atomic target via dissociation of NH_3.

Generation of bright deep-UV light sources is a long-standing challenge in laser science. Excimer lasers have been the workhorse solution for high average power deep-UV generation [8], and are widely used in industrial and medical applications [9]. However, their repetition rates and pulse duration are limited to few kilohertz nanosecond pulses.

Alternatively, nonlinear frequency conversion of high-power near-infrared lasers enables tabletop laser systems with greater flexibility in repetition rate and pulse duration down to the femtosecond regime. This potential can be seen by the impressive third-harmonic generation results at 343 nm of up to 234 W average power with 8 ps pulses and 300 kHz repetition rate [10] and 100 W with 730 fs pulses at 3.5 MHz [11]. However, in the deep-UV, efficient operation of nonlinear crystals becomes much more challenging. The highest average power solid-state picosecond source in the deep-UV at wavelengths shorter than 240 nm was reported by HiLASE [12–14], where up to 0.8 W output of deep-UV light at 206 nm was achieved by fifth-harmonic generation of a 60 W, 4 ps thin disk regenerative amplifier at 1030 nm.

Average power scaling of picosecond deep-UV sources has been limited by three central issues: dispersion, multiphoton absorption, and damage. In this article, we present a general scheme to overcome these challenges and thereby achieve efficient generation of deep-UV radiation at 206 nm from a 1030 nm 2 ps pump laser. We demonstrate picosecond pulses with record-high 2.5 W average power at a repetition rate of 100 kHz.

2. CONCEPTUAL DESIGN

Two-photon absorption (TPA) and crystal degradation are common problems in the deep-UV spectral range. A performance decrease after several (hundred) hours of operation due to color center formation has been repeatedly reported [15]. Additionally,

absorption causes temperature gradients inside the crystal and thermal dephasing. Both, the two-photon absorbed intensity and crystal degradation, are intensity dependent with a quadratic scaling for TPA, $\frac{d}{dz}I_{tpa} = -\beta_{tpa} \cdot I^2$ [16]. The deep-UV generation scheme needs to account for that in order to limit negative effects to a tolerable level. Using longer crystals and lower intensities is beneficial since this favors the $\chi^{(2)}$ process over the $\chi^{(3)}$ process such as TPA. However, the increased material dispersion at shorter wavelengths favors shorter nonlinear crystals and higher intensities when working with short pulses in the deep-UV. Thus, TPA implies a trade-off between bandwidth and efficiency.

Broadband phase matching methods have been introduced to overcome this fundamental trade-off. Examples include pulse front tilted optical parametric amplification [17], achromatic frequency doubling [18,19], frequency domain nonlinear optics [20], and gas phase nonlinear optics in hollow fibers [21]. However, such methods have not been demonstrated in the context of high-power deep-UV generation, where the thermal effects associated with multiphoton absorption are especially critical. Here we leverage the general method of group velocity matched three-wave mixing [22] to achieve efficient and high-power fifth-harmonic generation.

The choice of the nonlinear crystal is critical. Among the common deep-UV crystals CsLiB$_6$O$_{10}$ (CLBO) and $\beta-$BaB$_2$O$_4$ (BBO), we chose BBO because of a higher effective nonlinear coefficient d_{eff} and a lower TPA cross section ($d_{eff} = 1.97$ pm V^{-1} for collinear configuration, $\beta_{248\,nm} = 0.34 \pm 0.09$ cm GW^{-1}) compared to CLBO ($d_{eff} = 1.03$ pm V^{-1} for collinear configuration, $\beta_{248\,nm} = 0.53 \pm 0.12$ cm GW^{-1}) [23–25]. BBO is also favorable in terms of its hygroscopic properties. On the other hand, BBO features a larger temporal walk-off leading to a reduced spectral acceptance bandwidth, and a larger spatial walk-off leading to a reduced angular acceptance bandwidth. To produce deep-UV light from a 1 µm pump laser, we use sum-frequency generation (SFG) of $1\omega + 4\omega$, because this type of SFG offers a much larger effective nonlinearity ($d_{eff} = 1.97$ pm V^{-1}) in comparison to the alternative $2\omega + 3\omega$ scheme ($d_{eff} = 0.72$ pm V^{-1}). This difference is due to the decreasing value of d_{eff} with respect to the phase matching angle, in combination with the smaller phase matching angle required for the $1\omega + 4\omega$ case (54.2°) compared to the $2\omega + 3\omega$ case (77.1°). Note, these angles correspond to a collinear arrangement, and our calculations of d_{eff} use the Miller rule for the wavelength dependence of $\chi^{(2)}$.

3. GROUP VELOCITY MATCHING AND TILTED PULSE FRONTS

The overall optical design follows from the most crucial part, the SFG stage, which sets the requirements to the preceding conversion steps.

TPA and crystal degradation require comparably long crystals with a large aperture to make up for the low intensity. However, in BBO, there is a large group velocity mismatch (GVM) between the 1ω and 4ω, equal to 1.33 ps mm^{-1} for standard type-I SFG. Consequently, temporal overlap is lost after ≈ 1 mm, which is incompatible with the low intensity approach. Hence, a scheme for matching both phase and group velocity is required. A noncollinear arrangement in combination with a pulse front tilt (PFT) on the mixing waves allows for the effective group velocity matching in propagation direction [26]. The PFT angles of all involved waves inside the crystal need to be carefully matched to obtain overlap throughout the large beam profiles.
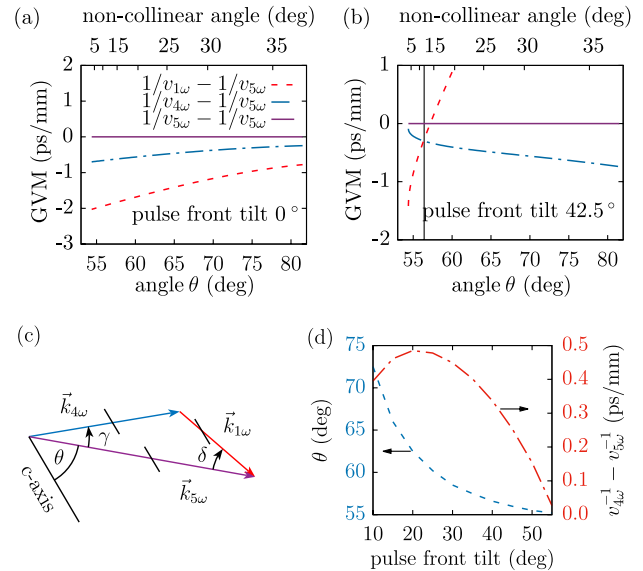

Fig. 1. Group velocity mismatch (GVM) as a function of the BBO crystal angle with respect to the generated fifth harmonic with an internal pulse front tilt of (a) 0° and (b) 42.5° of the fifth harmonic. The top axis shows the corresponding internal noncollinear angle between the fundamental and fourth harmonic ($\gamma + \delta$) that leads to phase matching at the corresponding crystal angle. Calculations according to SNLO at 400 K. (c) $\vec{k}$ vector diagram for noncollinear sum-frequency generation with matched pulse front tilts. The angles γ and δ denote the noncollinear angles of the generating waves ω and 4ω with respect to the generated 5ω wave, and θ the phase matching angle. (d) Group velocity mismatch between the fundamental and the 4ω wave as a function of the applied internal pulse front tilt; for each PFT value, we choose the optimum θ to minimize GVM, as described in the text.

The numeric values for the crystal cut angle θ, the noncollinear angle, and the amount of PFT required in the SFG process (5ω generation) were determined using the SNLO software package (v 68.2.0), which implements the calculations of [26]. Figures 1(a) and 1(b) show the obtained GVM in BBO as a function of θ, for PFT angles of 0° and 42.5°. Note, the figures show the value of $v_{n\omega}^{-1} - v_{5\omega}^{-1}$ for $n = 1$ (fundamental), $n = 4$ (fourth harmonic), and $n = 5$ (fifth harmonic). The angle convention used is illustrated in Fig. 1(c). The GVM remains large for any noncollinear angle in the absence of a PFT as can be seen in Fig. 1(a). In contrast, when a large PFT is employed as in Fig. 1(b), both GVM curves reach a small GVM value at modest noncollinear angles. In both cases, the crystal cut angle θ (lower horizontal axis) increases monotonically with noncollinear angle (upper horizontal axis). In Fig. 1(b), the 1ω and 4ω GVM curves cross at $\theta \approx 56°$. This point represents an optimum in terms of GVM, since all three waves have a similar group velocity. This optimal crystal cut angle depends on the PFT. Hence, in order to determine the optimum PFT, in Fig. 1(d), we show the optimal crystal cut and corresponding GVM as a function of the PFT angle.

The value of d_{eff} decreases with increasing θ, becoming negligible at $\theta = 90°$. Using a large PFT angle shifts the GVM crossing point to small values of θ, thereby maximizing the nonlinear coefficient. On the other hand, larger values of PFT are more challenging to implement and manage in the optical setup. On this basis, we decided that the best trade-off for the design parameters is an internal PFT angle of 42.5° for the 5ω wave, a noncollinear angle of $\gamma + \delta = 11.8°$ between the 1ω and 4ω waves, and a
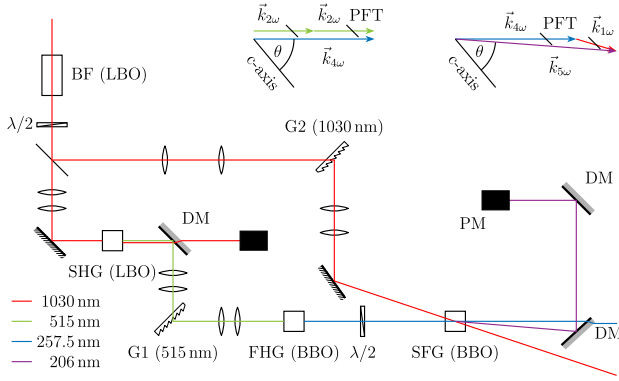
Fig. 2. Schematic of the optical design for frequency conversion to the fifth harmonic via sum-frequency generation (SFG) including cascaded $\chi^{(2)}$ beam flattening (BF), second-harmonic generation (SHG), fourth-harmonic generation (FHG), and introduction of pulse front tilts via diffraction gratings (G1, G2). The residual fundamentals in the different frequency conversion stages are filtered with dichroic mirrors (DMs). The pairs of lenses indicate elliptical beam shaping with reimaging between the labeled subsequent nonlinear crystals and gratings. The insets at the top center and top right depict, respectively, the k-vector diagram for the FHG and SFG stage including the pulse front tilt (PFT).
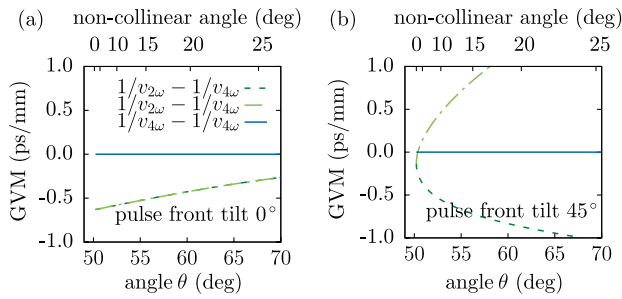

Fig. 3. Group velocity mismatch (GVM) as a function of the crystal rotation angle θ with respect to the generated fourth-harmonic beam for the two cases of internal pulse front tilt of (a) 0° and (b) 45° of the fourth harmonic. The corresponding internal noncollinear angle between the two incident 2ω beams for optimal phase matching is indicated on the top axis.

crystal cut angle of $\theta = 56.4°$ with respect to the generated 5ω wave [cf. Fig. 1(c)]. This noncollinear arrangement results in $d_{\text{eff}} = 1.88 \text{ pm V}^{-1}$ (collinear case $d_{\text{eff}} = 1.97 \text{ pm V}^{-1}$). For these values, the difference in group delay between the mixing waves is $v_{4\omega}^{-1} - v_{5\omega}^{-1} = v_{1\omega}^{-1} - v_{5\omega}^{-1} = -0.3 \text{ ps mm}^{-1}$, which is more than 6 times smaller than without the group velocity matching approach $(v_{1\omega}^{-1} - v_{5\omega}^{-1} = -2.0 \text{ ps mm}^{-1})$, which ensures temporal overlap throughout the crystal length. Obtaining such PFT on the 5ω wave requires suitably tilted pulse fronts of the input waves to the SFG crystal: the free-space (internal) PFT of the 1ω and 4ω beams must be 64.7° (52.1°) and 60.4° (40.3°), respectively.

Our experimental system layout is shown in Fig. 2. The PFT is introduced via diffraction gratings G1 and G2 [27] for both the 1ω and the 4ω beam. For the 1ω beam, the PFT is applied directly via G2. For the 4ω beam, the PFT is already introduced on the 2ω beam by G1 and subsequently transferred to the 4ω beam in the fourth-harmonic generation (FHG) stage. This approach is beneficial since it greatly reduces the GVM also in the collinear FHG stage [22] (cf. Fig. 3), as well as the number of optical elements

exposed to deep-UV radiation. The change of wavelength and the transition from the extraordinary axis in the FHG stage to the ordinary axis in the SFG stage affects the PFT angle and needs to be corrected for. Hence, a free-space PFT of 59.8° is required at the input to the $2\omega \rightarrow 4\omega$ frequency conversion. Note that all values are calculated at a BBO crystal temperature of 400 K.

4. BEAM FLATTENING FOR UNIFORM, EFFICIENT THREE-WAVE MIXING

Spatially and temporally inhomogeneous beam profiles are one of the main reasons for limited conversion efficiencies of nonlinear stages. Various beam-flattening schemes exist to achieve more uniform conversion through shaping of the spatiotemporal profile [28]. Here, we present a flattening scheme offering low losses and high robustness to changes on the wavefront of the input beam that occur due to long-term drifts in the commercial pump laser.

We employ a cascaded nonlinear $\chi^{(2)}$ flattening scheme in an antireflection-coated lithium triborate (LBO) crystal to shape the incoming pump beam for maximum conversion efficiencies of the subsequent nonlinear stages. In this scheme, a phase mismatch Δk in a second-harmonic (SH) conversion process translates into a negative (or positive) effective nonlinear refractive index [29],

$$n_{2,\text{eff}} = n_{2,\text{intrinsic}} - \frac{1}{\Delta k} \frac{4\pi d_{\text{eff}}^2}{\epsilon_0 c \, n_{\text{FW}}^2 n_{\text{SH}} \lambda_{\text{FW}}}, \quad (1)$$

which is composed of the intrinsic $\chi^{(3)}$ contribution $n_{2,\text{intrinsic}} = 1.9 \times 10^{-16} \text{ cm}^2 \text{ W}^{-1}$ [30] and a contribution from the phase mismatched $\chi^{(2)}$ process. n_{FW} and n_{SH} are the refractive indices of the fundamental wave (FW) and SH wave, respectively, and λ_{FW} denotes the wavelength of the fundamental. The magnitude of the phase mismatch $\Delta k = k_{\text{SH}} - 2k_{\text{FW}}$ and thus the flattening can be tuned by controlling the crystal temperature [31]. Operating the 15 mm long LBO crystal ($\theta = 90°$, $\phi = 0°$) at 120°C, i.e., somewhat below the second-harmonic generation (SHG) noncritical phase matching temperature for 1030 nm of $T = 194°C$, yields a phase mismatch of $\Delta k = 9.14 \text{ mm}^{-1}$ and a total $n_{2,\text{eff}} \approx -6.7 \times 10^{-16} \text{ cm}^2 \text{ W}^{-1}$.

In conclusion, propagation through this configuration induces a self-defocusing Kerr-lens with negligible losses. After free-space propagation, this intensity-dependent lens can transform an initially Gaussian-like beam into a flattened beam profile. More intense parts of the pulse in time experience a stronger defocusing effect, thereby clamping the intensity across the spatiotemporal distribution of the beam, as simulated in Figs. 4(a) and 4(b).

Based on the beam size measured before the setup and the scaling factor of a telescope before the beam-flattening crystal, we estimate a $1/e^2$ beam radius between 600 and 700 μm at the LBO crystal. To simulate the flattening effect, we use a symmetric Gaussian input beam with waist $w = 650$ μm and a sech^2-pulse in time domain of duration 1.57 ps. We calculate the peak intensity according to $I_{\text{pk}} = 0.8 \times P_{\text{av}}/((\pi/2)w^2 T_{\text{FWHM}} f_{\text{rep}}) = 50 \text{ GW cm}^{-2}$, where average power $P_{\text{av}} = 65$ W, $T_{\text{FWHM}} = 2$ ps, $f_{\text{rep}} = 100$ kHz, and the factor of 0.8 accounts for third-order dispersion (TOD) effects on the 1030 nm pulse shape. At propagation distance zero, i.e., the exit of the LBO crystal, we apply a nonlinear phase proportional to the laser intensity, with a maximum self-phase modulation (SPM) of −3.06 rad at the peak in space and time. We propagate the beam after the crystal using Fourier optics.
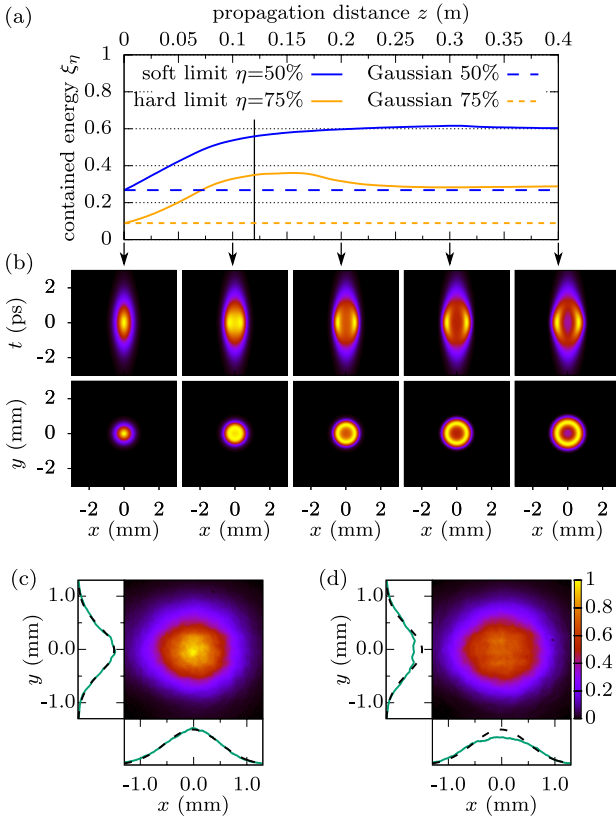
Fig. 4. (a) Evolution of energy abundance contained in a 2D Gaussian beam with $sech^2$ temporal shape after undergoing $\chi^{(2)}$ beam flattening. The solid blue and yellow lines represent the contained energy fraction of the pulse with a 50% and 75% threshold (peak intensity), respectively, in contrast to the nonflattened case depicted by the corresponding dashed lines [see Eq. (2)]. (b) Temporal (slice at $y = 0$) and spatial (slice at $t = 0$) evolution of the beam profile after $\chi^{(2)}$ beam flattening. The vertical black line at 0.12 m indicates the reimaging point used in the experiment. (c) Flattening effect on pump beam, monitored with the time integrating beam profiling camera placed 12 cm after beam-flattening crystal at low power—no beam flattening; and (d) at high power (65 W, 1030 nm, 900 μm beam radius)—with significant flattening of the input beam. The pulse parameters used for the simulation resemble the ones in the experiment.

Figure 4(b) shows the simulated beam profile at several distances after the crystal. To evaluate the beam-flattening process, we note that only parts of the pulse where the intensity is sufficiently high contribute efficiently to nonlinear interactions. Hence, to obtain a metric for the fidelity of the flattening, we calculate the fraction of the pulse ξ where the intensity stays within a certain fraction η of the peak intensity,

$$\xi_\eta = \iiint_{I/\max(I)>\eta} I(x, y, t)\mathrm{d}x\mathrm{d}y\mathrm{d}t \Big/ \iiint I(x, y, t)\mathrm{d}x\mathrm{d}y\mathrm{d}t.$$
(2)

The results are shown in Fig. 4(a) for two clip levels ($\eta = 50\%$ and 75%). At a distance of 12 cm after the crystal, indicated by the vertical line in the figure, there is a factor of >2 improvement, and the corresponding beam [Fig. 4(b)] exhibits a clearly flattened shape. We chose this plane as the one to reimage for the subsequent harmonic generation stages (SHG, FHG, and SFG). In addition to reimaging, the corresponding lens system is optimized to yield

a flat wavefront at each of the nonlinear crystals. This proved to be crucial for reaching high efficiencies. The resulting experimentally measured incident beam profile on the SHG stage is shown in Fig. 4(c) at low power (unflattened) and in Fig. 4(d) at high power (flattened). Note that these beam profiles are time-integrated since they were measured on a camera. We validated experimentally that parasitic SHG in the beam-flattening crystal is negligible (<500 mW).

5. IMPLEMENTATION

A technical aspect we consider especially crucial is the angular acceptance range in the FHG and SFG stage, which requires precise tuning of the crystal rotation angle with an accuracy of 50 μrad and 100 μrad, respectively. A deviation from the ideal crystal rotation angle by this amount corresponds to a decrease of approx. 5% in output power. We use piezo-actuated rotation stages (SmarAct GmbH, accuracy of 1 μrad) to achieve this precision, which have proven invaluable to correct for thermalization effects occurring during the first 30 s of full power operation.

Likewise, the phase matching in the FHG and SFG stage is temperature sensitive, and active stabilization down to 0.1 K is needed. The crystal oven is an in-house development to ensure one-dimensional (1D) heat extraction on both sides along the short (vertical) axis of the crystal. Both FHG and SFG crystals are permanently stabilized at 100°C to prevent degradation of the uncoated hygroscopic BBO facets due to humidity. The crystals are wrapped in indium foil before being placed into the copper crystal ovens. Thermal contact is made between the 20-mm-wide sides of the crystal (top and bottom facets) and the mount. This, in combination with elliptical beams filling most of the available crystal aperture, yields efficient heat flow, which is close to 1D along the short (vertical) axis of the crystal. This approach mitigates the influence of self-heating of the crystal by absorption of the laser beams.

We use two custom transmission gratings (Wasatch Photonics) with a groove density N of 2850 l/mm and 1400 l/mm for the 515 nm and 1030 nm beam, respectively. The gratings are designed to introduce the desired PFT, α_t, at Littrow condition, thereby maximizing the diffraction efficiency into the first order (94% for 515 nm and 99% for 1030 nm, both optimized for horizontal polarization). At Littrow condition, the grating equation for the first diffraction order simplifies to $\sin\varphi = \frac{\lambda N}{2}$, where φ is the diffraction angle as a function of the wavelength λ. Following [32], the angular dispersion introduced by the grating corresponds to a PFT angle α_t, which is given by

$$\tan\alpha_t = \lambda_0 \frac{d\varphi}{d\lambda}\Big|_{\lambda_0}.$$
(3)

To eliminate the evolution of spatial chirp after propagation of the beams, the grating planes are reimaged to the SFG crystal. A telescope in the 515 nm path allows us to precisely match the PFT of the 257 nm beam to the 1030 nm one.

In the FHG and SFG stage, we use uncoated large-aspect-ratio crystals (20×4 mm^2) (Eksma Optics) and elliptical beam shapes (11.4×2.6 mm^2 FWHM) to obtain an approximately 1D heat flow between crystal and oven. This facilitates heat extraction, which is crucial for deep-UV power scaling.

The FHG and SFG stages are fully contained and immersed in a nitrogen environment to avoid degradation of optical surfaces by

ozone (O_3) and other radicals, byproducts of deep-UV absorption in ambient air.

6. DEEP-UV GENERATION RESULTS

In a first round of experiments, described in this section, we used 5-mm-long BBO crystals for deep-UV generation showing internal conversion efficiencies of up to 48.4% and an average power of up to 2.0 W at 206 nm. In a subsequent improvement, described in Section 7, we further optimized the crystal lengths and temporal pump shaping and obtained up to 2.5 W average power.

The deep-UV source (Fig. 2) is driven by an Yb^{3+}:YAG amplifier system (Amphos A400 + grating compressor). The system delivers pulses with a FWHM bandwidth of 0.8 nm centered around 1030 nm, which are intentionally chirped to ≈ 2 ps to drive OPCPA systems [33,34]. The amplifier system operates at 100 kHz repetition rate and delivers an average power of up to 280 W. For deep-UV generation, we use 65 W of the total available pump power. The input beam to the frequency conversion setup is continuously stabilized in position and angle (TEM Aligna 4D). After spatiotemporal beam flattening of the input beam, 55 W are reimaged into a 5-mm-long temperature-stabilized antireflection-coated LBO crystal for SHG ($\theta = 90°$, $\phi = 12.8°$, $T = 50°C$). A magnification factor of 1.33 between the beam flattening and the SHG crystal gives a flattened beam size at the SHG crystal of 1.3 mm × 1.4 mm FWHM. The SHG process yields 32.8 W of average power in the green (515 nm) with an efficiency of 60%. The generated SH inherits the flattened profile of the fundamental and is consequently reimaged onto the grating G1 and from there into the FHG and SFG stages.

The collinear FHG stage employs type-I (oo → e) birefringent phase matching in a 5-mm-long BBO crystal (Eksma Optics), where up to 5.1 W of the fourth harmonic (257.5 nm) are generated from a maximum pump power of 15.5 W. Corrected for the Fresnel losses of the uncoated crystal, this corresponds to an internal conversion efficiency of 40.6%, as shown in Fig. 5(a). The peak intensity of the 2ω and 4ω beam is estimated to be smaller than 200 MW cm^{-2} and 80 MW cm^{-2}, respectively. Separation of the collinearly propagating SH pump and the generated fourth harmonic is realized by a set of two dichroic mirrors (Layertec GmbH) achieving a reflection ratio 2ω to $4\omega < 1 : 10000$.

Last, the fifth harmonic is obtained from the generated fourth harmonic and the remaining 10 W of fundamental light transmitted through the beam-flattening crystal. SFG is performed in a 5-mm-long BBO crystal identical to the one used in the FHG stage. The phase matching scheme is again of birefringent type-I (oo → e). This requires a $\lambda/2$-waveplate to rotate the polarization state of the 4ω beam by 90° before entering the SFG stage. The group velocity matching scheme illustrated in Figs. 1 and 2 requires
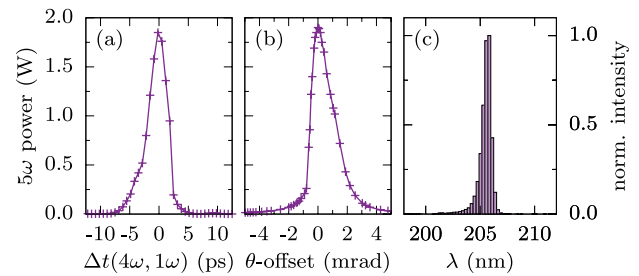
Fig. 6. Characterization of the SFG output at 2 W average power: (a) cross-correlation signal of the 4ω and 1ω beam, (b) output power versus crystal angle θ offset, and (c) spectrum of the generated output.

elliptical shaping and reimaging of the flattened fundamental profile on the grating G2 and from there into the SFG crystal. After spatial separation of the fundamental and filtering of the remaining fourth harmonic with two dichroic mirrors (Layertec GmbH, $R_p = 94\%$ at 206 nm and $T_s < 5\%$ at 257 nm), we measure a total average power in the fifth harmonic of up to 2.0 W (up to 2.5 W after improvements). This corresponds to an internal conversion efficiency of 48.4% from the fourth to the fifth harmonic. The peak intensity of the 1ω, 4ω, and 5ω beam is estimated to be smaller than 210 MW cm^{-2}, 70 MW cm^{-2} and 40 MW cm^{-2}, respectively. The FHG and SFG conversion efficiency versus input power are shown in Fig. 5. Note that the curve for the SFG conversion efficiency versus power was recorded by starting from highest power and going toward lowest power, while keeping the crystal rotation angle θ fixed at the optimum value for high-power operation. The rapid decrease of the conversion efficiency at lower pump powers is due to a reduced thermal load from TPA affecting the optimal phase matching angle. The three consecutive conversion stages reach a combined internal conversion efficiency of $\eta_{\omega \to 2\omega} \cdot \eta_{2\omega \to 4\omega} \cdot \eta_{4\omega \to 5\omega} = 11.5\%$ (corrected for all Fresnel losses).

Figure 6 presents the characterization of the generated fifth-harmonic output. From the cross-correlation signal obtained by scanning the delay between the fundamental and the fourth harmonic, we estimate a pulse duration of approximately 2 ps for the fifth harmonic [Fig. 6(a)]. The asymmetry with respect to the delay is due to residual TOD on the pump pulse of about -1.7 ps^3. The pulses yield a spectrum centered at 206 nm where the measurement was limited by the spectrometer resolution [Fig. 6(c)]. The phase matching angle requires a fine control with a resolution of 50 μrad [Fig. 6(b)].

Figure 7 shows the beam profiles of the 4ω and 5ω beam at 2.2 W output power. The profiles were recorded in the near-field behind the generating crystals at approximately 15 cm (40 cm) distance for the 4ω (5ω) beam. Both profiles show clear signs of distortions, likely originating from self-heating of the crystal due to absorption, which leads to thermal lensing and thermal dephasing effects. The thermally induced changes become visible around 1 W of 5ω output power and become stronger as the pump power is increased further until the maximum power of 2.5 W is reached. We observe a delayed response of the beam profile to sudden changes in pump power, which confirms the thermal origin of the distortions. The beam profile in (b) exhibits a fan-out on the left side whose cause is unclear. Important steps to improve the beam profile in the future would include: more homogeneous nonlinear crystals with minimal linear absorption coefficient; a more
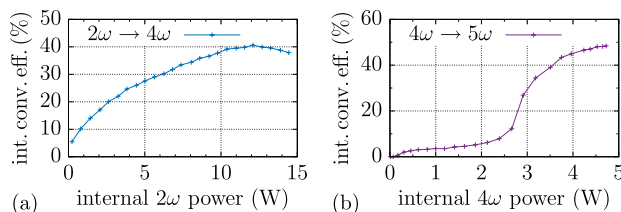

Fig. 5. Internal conversion efficiencies of the (a) fourth-harmonic generation and (b) fifth-harmonic sum-frequency generation as a function of the corresponding pump power.
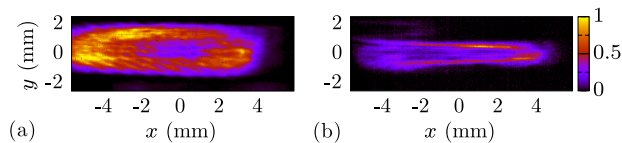
Fig. 7. Near-field beam profiles at 2.2 W output power of (a) the generated 257 nm beam measured ~15 cm after the crystal, and (b) the 206 nm beam at ~40 cm after the crystal.
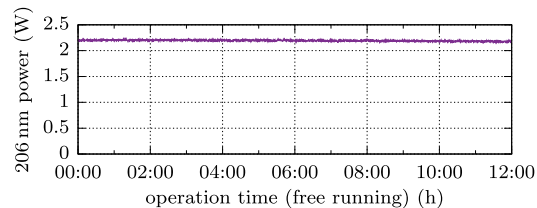

Fig. 8. Power stability measurement at 2.2 W over 12 h for the 5ω output at 206 nm.

uniform intensity distribution in the crystal (ideally a rectangular profile instead of elliptical); improved pump beam quality (our 1030 nm pump has $M^2 > 1.7$); a higher aspect ratio of the crystals; longitudinal temperature optimization [35]; and optimal crystal orientation with respect to the anisotropic thermal conductivity of BBO [36].

The group velocity matching approach that we apply here implies that the generated 206 nm beam carries a PFT of 57.9° in free space. The impact of the PFT on focal spot size and pulse duration can be described analytically for a given focusing geometry as derived in Ref. [32]. It would be possible to remove the PFT by reflecting the 206 nm beam on a suitable diffraction grating.

7. POWER OPTIMIZATION

Further power scaling from 2 W to 2.5 W average output power at 206 nm was enabled by two measures. First, improvements to the grating compressor of the pump laser enabled its temporal shape to be improved: the TOD was reduced from about $-1.7\,\mathrm{ps}^3$ to $-0.6\,\mathrm{ps}^3$. Second, the crystal length in the FHG stage was reduced from 5 mm to 3 mm to reduce the roll-over in conversion efficiency visible in Fig. 5(a). We tested three different crystal lengths (3, 4, and 5 mm) to find the best compromise between driving field intensity and crystal length yielding the highest average output power using the full available 32.5 W 515 nm pump power in the FHG stage.

Additionally, for an output power of 2.2 W, we measured an excellent stability of the source over more than 12 h of free-running operation with a root mean square error (RMSE) of 0.01 W (thermal detector, Gentec UP19K-30 H-H5-INT-D0), cf. Fig. 8. So far, further power scaling is limited by TPA in the FHG stage, resulting in beam distortions and hampered phase matching.

8. SUMMARY AND OUTLOOK

We demonstrated long-term stable high-power deep-UV generation from 2 ps pulses at 100 kHz repetition rate exceeding 2.5 W of average power. Since it is possible to fully equalize the velocities of the interacting waves with our approach, it is highly promising for

further scaling of deep-UV generation into the femtosecond pulse regime at high power, where GVM normally poses an even more severe limit. The ultimate limits will still be connected with TPA, and this could be addressed by improved heat management, use of longer crystals with minimized linear absorption, or use of crystals with lower nonlinear absorption cross sections.

Disclosures. The authors declare no conflicts of interest.

†These authors contributed equally to this paper.

REFERENCES

1. P. Herman, R. Marjoribanks, A. Oettl, K. Chen, I. Konovalov, and S. Ness, "Laser shaping of photonic materials: deep-ultraviolet and ultrafast lasers," Appl. Surf. Sci. **154-155**, 577–586 (2000).
2. G. Raciukaitis and M. Gedvilas, "Processing of polymers by UV picosecond lasers," in *24th International Congress on Applications of Lasers & Electro-Optics (ICALEO)* (2005), pp. 191–199.
3. R. Srinivasan, "Ablation of polymers and biological tissue by ultraviolet lasers," Science **234**, 559–565 (1986).
4. T. Kobayashi and Y. Kida, "Ultrafast spectroscopy with sub-10 fs deep-ultraviolet pulses," Phys. Chem. Chem. Phys. **14**, 6200–6210 (2012).
5. D. Sertore, S. Schreiber, K. Floettmann, F. Stephan, K. Zapfe, and P. Michelato, "First operation of cesium telluride photocathodes in the TTF injector RF gun," Nucl. Instrum. Methods Phys. Res. A **445**, 422–426 (2000).
6. P. Eckle, M. Smolarski, P. Schlup, J. Biegert, A. Staudte, M. Schöffler, H. G. Muller, R. Dörner, and U. Keller, "Attosecond angular streaking," Nat. Phys. **4**, 565–570 (2008).
7. P. Eckle, A. N. Pfeiffer, C. Cirelli, A. Staudte, R. Dörner, H. G. Muller, M. Büttiker, and U. Keller, "Attosecond ionization and tunneling delay time measurements in helium," Science **322**, 1525–1529 (2008).
8. D. Basting and G. Marowsky, *Excimer Laser Technology* (Springer, 2005).
9. N. Savage, "Ultraviolet lasers," Nat. Photonics **1**, 83–85 (2007).
10. J.-P. Negel, A. Loescher, A. Voss, D. Bauer, D. Sutter, A. Killi, M. A. Ahmed, and T. Graf, "Ultrafast thin-disk multipass laser amplifier delivering 1.4 kW (4.7 mJ, 1030 nm) average power converted to 820 W at 515 nm and 234 W at 343 nm," Opt. Express **23**, 21064–21077 (2015).
11. J. Rothhardt, C. Rothhardt, M. Müller, A. Klenke, M. Kienel, S. Demmler, T. Elsmann, M. Rothhardt, J. Limpert, and A. Tünnermann, "100 W average power femtosecond laser at 343 nm," Opt. Lett. **41**, 1885–1888 (2016).
12. O. Novák, H. Turčičová, M. Smrž, T. Miura, A. Endo, and T. Mocek, "Picosecond green and deep ultraviolet pulses generated by a high-power 100 kHz thin-disk laser," Opt. Lett. **41**, 5210–5213 (2016).
13. H. Turčičová, O. Novák, L. Roskot, J. Muzik, M. Smrž, A. Endo, and T. Mocek, "Picosecond deep ultraviolet pulses generated by a 100 kHz thin-disk laser system," Proc. SPIE **11042**, 110420H (2019).
14. H. Turcicova, O. Novak, L. Roskot, M. Smrz, J. Muzik, M. Chyla, A. Endo, and T. Mocek, "New observations on DUV radiation at 257 nm and 206 nm produced by a picosecond diode pumped thin-disk laser," Opt. Express **27**, 24286–24299 (2019).
15. S. C. Kumar, J. C. Casals, J. Wei, and M. Ebrahim-Zadeh, "High-power, high-repetition-rate performance characteristics of β-BaB$_2$O$_4$ for single-pass picosecond ultraviolet generation at 266 nm," Opt. Express **23**, 28091–28103 (2015).

16. R. W. Boyd, *Nonlinear Optics*, 3rd ed. (Academic, 2008).

17. A. Shirakawa, I. Sakane, M. Takasaka, and T. Kobayashi, "Sub-5-fs visible pulse generation by pulse-front-matched noncollinear optical parametric amplification," Appl. Phys. Lett. **74**, 2268–2270 (1999).

18. V. Volosov and E. Goryachkina, "Compensation of phase-matching dispersion in generation of nonmonochromatic radiation harmonics. I. Doubling of neodymium-glass radiation frequency under free-oscillation conditions," Sov. J. Quantum Electron. **6**, 854–857 (1976).

19. O. E. Martinez, "Achromatic phase matching for second harmonic generation of femtosecond pulses," IEEE J. Quantum Electron. **25**, 2464–2468 (1989).

20. B. E. Schmidt, N. Thiré, M. Boivin, A. Laramée, F. Poitras, G. Lebrun, T. Ozaki, H. Ibrahim, and F. Légaré, "Frequency domain optical parametric amplification," Nat. Commun. **5**, 3643 (2014).

21. F. Köttig, F. Tani, C. M. Biersach, J. C. Travers, and P. St. J. Russell, "Generation of microjoule pulses in the deep ultraviolet at megahertz repetition rates," Optica **4**, 1272–1276 (2017).

22. R. Danielius, A. Piskarskas, P. D. Trapani, A. Andreoni, C. Solcia, and P. Foggi, "Matching of group velocities by spatial walk-off in collinear three-wave interaction with tilted pulses," Opt. Lett. **21**, 973–975 (1996).

23. R. C. Eckardt, H. Masuda, Y. X. Fan, and R. L. Byer, "Absolute and relative nonlinear optical coefficients of KDP, KD*P, BaB_2O_4, $LiIO_3$, $MgO:LiNbO_3$, and KTP measured by phase-matched second-harmonic generation," IEEE J. Quantum Electron. **26**, 922–933 (1990).

24. I. Shoji, H. Nakamura, R. Ito, T. Kondo, M. Yoshimura, Y. Mori, and T. Sasaki, "Absolute measurement of second-order nonlinear-optical coefficients of for visible-to-ultraviolet second-harmonic wavelengths," J. Opt. Soc. Am. B **18**, 302–307 (2001).

25. G. Kurdi, K. Osvay, J. Klebniczki, M. Divall, E. J. Divall, A. Péter, K. Polgár, and J. Bohus, "Two-photon-absorption of BBO, CLBO, KDP and LTB crystals," in *Advanced Solid-State Photonics* (Optical Society of America, 2005), paper MF18.

26. A. V. Smith, "Group-velocity-matched three-wave mixing in birefringent crystals," Opt. Lett. **26**, 719–721 (2001).

27. A. V. Smith, *Crystal Nonlinear Optics: With SNLO Examples* (AS-Photonics, 2015).

28. J. Moses and S.-W. Huang, "Conformal profile theory for performance scaling of ultrabroadband optical parametric chirped pulse amplification," J. Opt. Soc. Am. B **28**, 812–831 (2011).

29. G. I. Stegeman, D. J. Hagan, and L. Torner, "$\chi^{(2)}$ cascading phenomena and their applications to all-optical signal processing, mode-locking, pulse compression and solitons," Opt. Quantum Electron. **28**, 1691–1740 (1996).

30. M. Sheik-Bahae and M. Ebrahimzadeh, "Measurements of nonlinear refraction in the second-order $\chi^{(2)}$ materials $KTiOPO_4$, $KNbO_3$, β-BaB_2O_4, and LiB_3O_5," Opt. Commun. **142**, 294–298 (1997).

31. K. Kato, "Temperature-tuned 90° phase-matching properties of LiB_3O_5," IEEE J. Quantum Electron. **30**, 2950–2952 (1994).

32. G. Pretzler, A. Kasper, and K. Witte, "Angular chirp and tilted light pulses in CPA lasers," Appl. Phys. B **70**, 1–9 (2000).

33. N. Bigler, J. Pupeikis, S. Hrisafov, L. Gallmann, C. R. Phillips, and U. Keller, "High-power OPCPA generating 1.7 cycle pulses at 2.5 µm," Opt. Express **26**, 26750–26757 (2018).

34. J. Pupeikis, P.-A. Chevreuil, N. Bigler, L. Gallmann, C. R. Phillips, and U. Keller, "Water window soft x-ray source enabled by a 25 W few-cycle 2.2 µm OPCPA at 100 kHz," Optica **7**, 168–171 (2020).

35. S. Ghavami Sabouri and A. Khorsandi, "Active control of thermal dephasing effect in high power continuous wave single-pass second harmonic generation," IEEE J. Quantum Electron. **51**, 1–8 (2015).

36. R. Riedel, J. Rothhardt, K. Beil, B. Gronloh, A. Klenke, H. Höppner, M. Schulz, U. Teubner, C. Kränkel, J. Limpert, A. Tünnermann, M. Prandolini, and F. Tavella, "Thermal properties of borate crystals for high power optical parametric chirped-pulse amplification," Opt. Express **22**, 17607–17619 (2014).